ELECTROCHEMISTRY

Oxygen-deficient triple perovskites as highly active and durable bifunctional electrocatalysts for oxygen electrode reactions

Nam-In Kim[1], Young Jin Sa[2], Tae Sup Yoo[3], Sung Ryul Choi[1], Rana Arslan Afzal[1], Taekjib Choi[1], Young-Soo Seo[1], Kug-Seung Lee[4], Jun Yeon Hwang[5], Woo Seok Choi[3], Sang Hoon Joo[2]*, Jun-Young Park[1]*

Highly active and durable bifunctional oxygen electrocatalysts have been of pivotal importance for renewable energy conversion and storage devices, such as unitized regenerative fuel cells and metal-air batteries. Perovskite-based oxygen electrocatalysts have emerged as promising nonprecious metal bifunctional electrocatalysts, yet their catalytic activity and stability still remain to be improved. We report a high-performance oxygen electrocatalyst based on a triple perovskite, $Nd_{1.5}Ba_{1.5}CoFeMnO_{9-\delta}$ (NBCFM), which shows superior activity and durability for oxygen electrode reactions to single and double perovskites. When hybridized with nitrogen-doped reduced graphene oxide (N-rGO), the resulting NBCFM/N-rGO catalyst shows further boosted bifunctional oxygen electrode activity (0.698 V), which surpasses that of Pt/C (0.801 V) and Ir/C (0.769 V) catalysts and which, among the perovskite-based electrocatalysts, is the best activity reported to date. The superior catalytic performances of NBCFM could be correlated to its oxygen defect–rich structure, lower charge transfer resistance, and smaller hybridization strength between O 2p and Co 3d orbitals.

INTRODUCTION

Electrochemical energy conversion and storage devices based on the interconversion of the chemical energy of fuels and renewable electricity, such as fuel cells, water-splitting cells, and metal-air batteries, offer a sustainable solution in an era of global climate change (*1*). Oxygen electrode reactions—the oxygen evolution reaction (OER) and the oxygen reduction reaction (ORR)—are ubiquitous in renewable energy devices, and the catalysts for the OER and ORR significantly influence device performances. Since both the OER and ORR require a proton-coupled, four-electron transfer, the kinetics of these reactions are intrinsically sluggish (*2*). Currently, precious metal–based electrocatalysts are used predominantly as oxygen electrode catalysts, owing to their excellent activity (for example, Pt alloys for ORR and IrO_2 or RuO_2 for OER); however, precious metal catalysts are prohibitively expensive and scarce. Hence, the design of highly active, durable, and cost-efficient bifunctional oxygen electrode catalysts has been of pivotal importance in advancing electrochemical energy devices (*1*–*3*).

In this context, nonprecious metal–based bifunctional oxygen electrode catalysts have been widely pursued (*2*–*5*). Catalysts based on heteroatom-doped carbons and transition metal oxides have been at the forefront of this research (*3*–*5*). Doped carbon–based catalysts have often demonstrated remarkable ORR activity; however, they are subject to facile degradation under the highly corrosive operational potential of OER [>1.4 V versus reversible hydrogen electrode (RHE)]. In contrast, transition metal oxides are intrinsically more stable than carbon materials under OER conditions. Among various metal oxides, perovskites with the general formula of ABO_3 constitute a highly intriguing class of materials; they can host a myriad of compositions and structures, which, in turn, modulate their physicochemical and catalytic properties. Perovskites have recently been attracting renewed interest as bifunctional oxygen electrode catalysts (*4*–*11*). Toward the rational design of high-performance perovskite-based oxygen electrocatalysts, a number of important parameters affecting catalytic reactivity have been identified. The filling of e_g orbital in B-site metal has been uncovered as a descriptor for predicting activities for both the OER and ORR (*12*, *13*). The covalency between B-site metal and oxygen has also been proposed to exert a significant role in determining the oxygen electrode activities (*14*). On the basis of these principles, perovskite structures with pronounced catalytic activity for oxygen electrode reactions have been identified, including single perovskite, $Ba_{0.5}Sr_{0.5}Co_{0.8}Fe_{0.2}O_{3-\delta}$ (BSCF) (*12*), and double perovskite, $LnBaCo_2O_{5+\delta}$ (Ln = Pr, Nd, Sm, and Gd) (*14*). As another important determinant, oxygen vacancies have also been found to profoundly influence the catalytic activity and stability of perovskite-based catalysts for the OER and ORR (*15*). Crystal structures (*16*) and electrical conductivity (*17*) are also suggested as important factors that affect the catalytic performance. Although great advances have been achieved via engineering of the composition and defect chemistry in perovskite catalysts, further improvements in terms of activity and stability are essential for the design of advanced catalysts, as well as their widespread utility in electrochemical energy devices.

Here, we introduce a triple perovskite, $Nd_{1.5}Ba_{1.5}CoFeMnO_{9-\delta}$ (NBCFM), as a highly active and durable bifunctional oxygen electrocatalyst for the OER and ORR. The triple perovskite is defined as a structure related to cubic perovskite with one of the cubic axes (*c* axis) tripled (*18*), and the NBCFM structure can be generated by stacking three single perovskite blocks with the central Nd^{3+} and the top/bottom Ba^{2+} at the A site. Similarly, the unit cell of $LnBaCo_2O_{5+\delta}$ (double perovskite) is twice that of perovskite, and the substitution of the Ln^{3+} site by lower-valence Ba^{2+} generates a layered structure with the Nd^{3+} and Ba^{2+} alternating along the *c* direction (*14*). A few triple perovskites, with the notable example of $YBa_2Cu_3O_{7-\delta}$, have been designed for high-transition-superconducting material applications (*18*). However, to the best of our knowledge, triple perovskites have never been exploited as bifunctional oxygen electrode catalysts for both the OER and ORR. NBCFM

[1]Hybrid Materials Center, Department of Nanotechnology and Advanced Materials Engineering, Sejong University, Seoul 05006, Republic of Korea. [2]School of Energy and Chemical Engineering, Ulsan National Institute of Science and Technology, Ulsan 44919, Republic of Korea. [3]Department of Physics, Sungkyunkwan University, Suwon 16419, Republic of Korea. [4]Pohang Accelerator Laboratory, Pohang 37673, Republic of Korea. [5]Carbon Composite Materials Research Center, Institute of Advanced Composite Materials, Korea Institute of Science and Technology Jeonbuk Branch, Jeonbuk 55324, Republic of Korea.
*Corresponding author. Email: jyoung@sejong.ac.kr (J.-Y.P.); shjoo@unist.ac.kr (S.H.J.)

exhibited superior activity and durability for the OER and ORR to single perovskite (BSCF) and double perovskite [$NdBa_{0.5}Sr_{0.5}Co_{1.5}Fe_{0.5}O_{5+\delta}$ (NBSCF)] structures. NBCFM hybridized with nitrogen-doped reduced graphene oxide (NBCFM/N-rGO) showed further enhanced catalytic activities with excellent durability. The oxygen electrode activity (the potential gap between the OER potential at 10 mA cm^{-2} and the ORR potential at −3 mA cm^{-2}) of NBCFM/N-rGO was as small as 0.698 V. This activity is substantially better than those of Pt/C (0.801 V) and Ir/C (0.769 V) catalysts and, importantly, is the best performance reported to date among perovskite-based bifunctional oxygen electrocatalysts. A combination of characterizations suggests that the excellent catalytic performance of NBCFM could be ascribed to the structure enriched with oxygen defects, low charge transfer resistance, and small hybridization strength between O 2p and Co 3d orbitals.

RESULTS

Crystal structures and microstructures of the perovskite catalysts

Figure 1A shows the x-ray diffraction (XRD) patterns of the perovskite-based catalysts (BSCF, NBSCF, and NBCFM), together with their Rietveld refinement results. All observed XRD peaks of the catalysts are commensurate with perovskite structures, and no peaks for other phases are observed, indicating the high phase purity of the synthesized catalysts. The average crystallite sizes of BSCF, NBSCF, and NBCFM are calculated as 5.84, 4.82, and 4.83 nm, respectively, as determined by the Scherrer equation. The structural parameters of the perovskite catalysts calculated by the Rietveld refinements suggest that lattice constants of the three perovskites for *a* and *b* axes are nearly invariant, whereas their *c*-axis lattice constants progressively increase from 3.979 to 7.737 and to 11.676 Å for BSCF, NBSCF, and NBCFM, respectively (Fig. 1B and Table 1). Table 1 lists the structures (and space groups) of BSCF, NBSCF, and NBCFM, which are indexed as cubic ($Pm\bar{3}m$), orthorhombic (*Pmmm*), and tetragonal structures (*P4/mmm*), respectively. The structural deviations of NBSCF and NBCFM perovskites from the simple cubic structure originate from the lattice distortion and expansion phenomena by doping of lanthanide (A site) with transition metal (B site) in the perovskite system (*19*). In addition, to maintain charge neutrality of the perovskite system under the presence of multivalent metal species ($Co^{2+/3+/4+}$, $Fe^{2+/3+/4+}$, and $Mn^{2+/3+/4+}$), extra oxygen vacancies are created with the structural modifications in NBSCF and NBCFM (*20*). As shown in Fig. 1C, the repeated stacking of lanthanide causes a structural

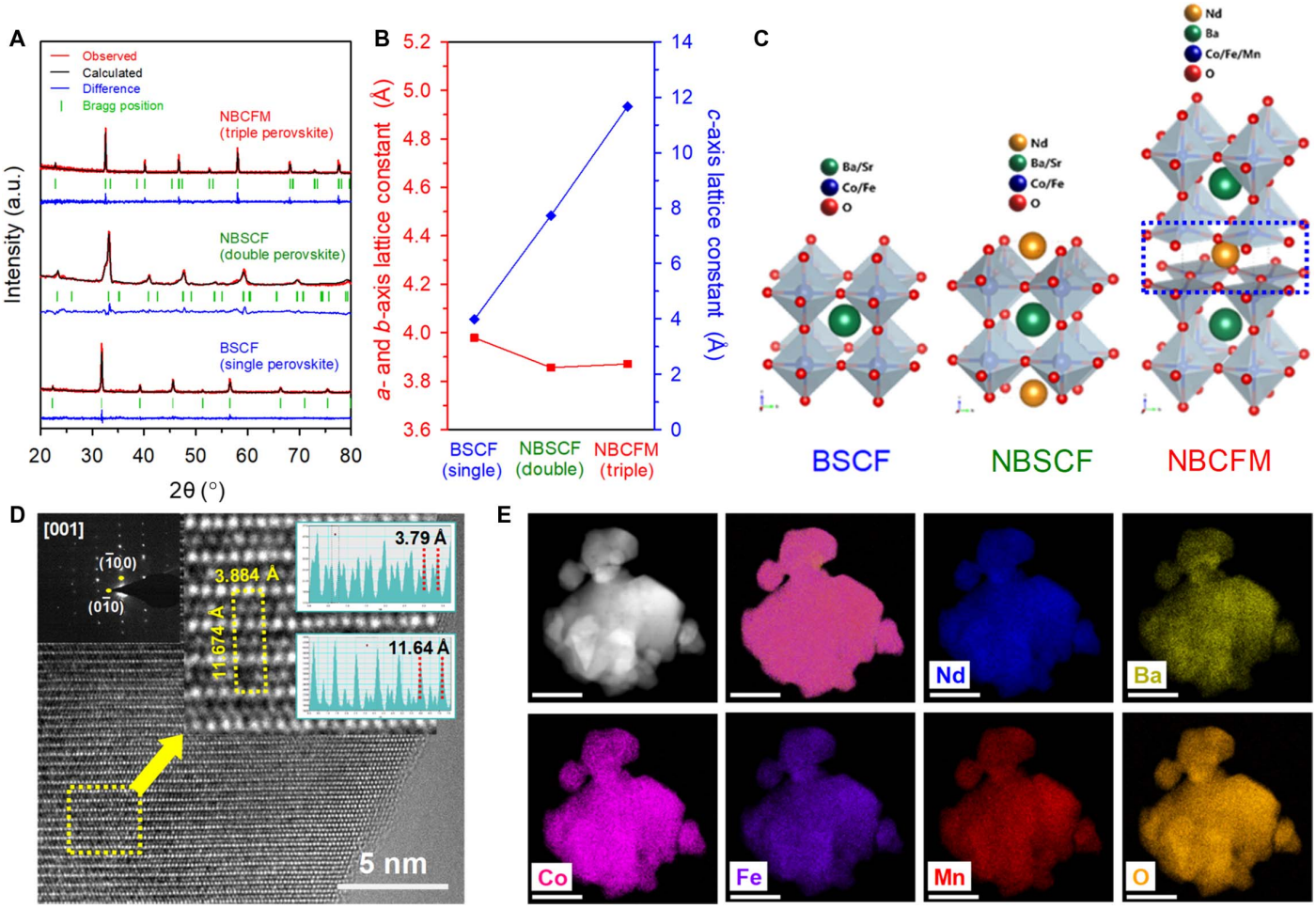

Fig. 1. Characterizations of the perovskite catalysts. (**A**) XRD patterns of BSCF, NBSCF, and NBCFM with their Rietveld refinement results. a.u., arbitrary units. (**B**) Lattice constants of the BSCF, NBSCF, and NBCFM (left, *a* and *b* axes; right, *c* axis). (**C**) Crystal structures of BSCF, NBSCF, and NBCFM. (**D**) HRTEM image of NBCFM catalyst with NBED pattern. Left inset shows the NBED pattern. Right inset shows an atomic resolution image of a yellow dotted rectangular section with an observed unit cell, its lattice parameters for *a* and *c* axes, and the line profile along *a* and *c* directions. (**E**) EDX elemental mapping results of NBCFM. Scale bars, 100 nm.

Table 1. Crystal-structural parameters of the catalysts from Rietveld refinement and the chemical titration method.

		BSCF (single perovskite)	NBSCF (double perovskite)	NBCFM (triple perovskite)
Space group		*Pm*$\bar{3}$*m*	*Pmmm*	*P4/mmm*
Phase structure		Cubic	Orthorhombic	Tetragonal
Lattice parameter	*a* (Å)	3.979	3.856	3.871
	b (Å)	3.979	3.827	3.871
	c (Å)	3.979	7.737	11.676
Unit cell volume (Å^3)		62.997	114.174	175.866
Oxygen deficiency, δ		0.234	0.379	0.495

distortion of the lattice in perovskite systems, generating extra oxygen vacancies via the structural deformation. These vacancies have been shown to play an important role in improving the catalytic activities for the OER and ORR (*21*), and this phenomenon will be discussed in the next section.

The formation of the triple perovskite structure in the NBCFM was further confirmed with nanobeam electron diffraction (NBED) pattern observed at the [001] zone axis of the high-resolution transmission electron microscopy (HRTEM) image (Fig. 1D). In the NBED pattern (Fig. 1D, left inset), representative points located next to the center can be indexed as $(\bar{1}00)$ and $(0\bar{1}0)$ reflections along the [001] zone axis of the NBCFM, indicating that NBCFM contains the {100} facet. The (100) plane of the NBCFM is well defined, and the average *a*- and *c*-axis lattice parameters are determined from the simulation of the relative intensity of each atomic column in the enlarged image (Fig. 1D, right inset). The atomic resolution image in the right inset shows that the NBCFM is exactly on the [001] zone axis, where the $(\bar{1}00)$ and $(0\bar{1}0)$ reflections are visible with the d_{111} = 3.884 Å (*a* and *b* axes) and d_{200} = 11.674 Å (*c* axis). These results indicate that the NBCFM has a trilayer of single perovskite structure, in agreement with the result of Rietveld refinements.

Field-emission scanning electron microscopy (FESEM) and TEM images of perovskite catalysts (fig. S1, A to F) show an agglomerated spherical particle morphology that ranges from 100 to 500 nm. Elemental mapping images of NBCFM sample based on energy-dispersive x-ray (EDX) spectroscopy (Fig. 1E and fig. S1, G to I) show that the constituent elements (Nd, Ba, Co, Fe, Mn, and O) are uniformly distributed throughout the particles, without any segregation. The porous nature of perovskites was investigated by nitrogen adsorption-desorption isotherms and their corresponding pore size distribution curves (fig. S2, A and B), and their Brunauer-Emmett-Teller (BET) surface areas are 12.3, 4.6, and 7.1 m^2 g^{-1} for BSCF, NBSCF, and NBCFM, respectively (table S1).

Electrocatalytic OER/ORR activity and stability of perovskite catalysts

The OER and ORR activities of perovskite catalysts were investigated by using rotating disk electrode (RDE) measurements in 0.1 M KOH solution (see Materials and Methods for details). Figure 2A shows the OER polarization curves of BSCF, NBSCF, and NBCFM catalysts. The triple perovskite NBCFM catalyst exhibits superior OER activity compared to other catalysts, with higher current density and lower overpotential (Fig. 2A and Table 2). The overpotential required for a current density of 10 mA cm^{-2} is 359 mV for NBCFM, which is significantly lower than that for BSCF (395 mV) and NBSCF (374 mV). The OER activity of the perovskites was further compared in terms of the specific activity, which was calculated by normalizing the current densities to the BET surface area, providing an activity metric of the catalyst surface. The calculated specific activity of NBCFM is 26.7 mA cm$^{-2}_{cat}$ at an overpotential of 350 mV, which is much greater than that of BSCF (6.7 mA cm$^{-2}_{cat}$) and NBSCF (21.7 mA cm$^{-2}_{cat}$). This indicates that these perovskites have more active surface toward the OER in the following order: triple > double > single. In the OER Tafel plots (Fig. 2A, inset, and Table 2), NBCFM shows a lower Tafel slope (81 mV decade^{-1}) than NBSCF (84 mV decade^{-1}) and BSCF (86 mV decade^{-1}), indicating the excellent intrinsic OER kinetics of NBCFM. For the ORR, NBCFM also exhibits the best activity among the three perovskite catalysts (Fig. 2B and fig. S3, A to C). NBCFM shows the highest half-wave potential (potential at −3 mA cm^{-2}) for the ORR at 0.698 V, followed by NBSCF (0.653 V) and BSCF (0.641 V). NBCFM also exhibits superior ORR kinetics to the other two catalysts, as revealed by Koutecky-Levich analysis (fig. S3, D to F). The electron transfer number of NBCFM is 3.9, which surpasses those of NBSCF (3.6) and BSCF (2.8). Tafel analysis for the ORR polarization curves (fig. S3, G to I) also supports the excellent ORR kinetics of NBCFM; the Tafel slope of NBCFM with 63 mV decade^{-1} is the lowest among the three perovskite catalysts. NBCFM's superior ORR kinetics could be further substantiated by its high diffusion-limited current density of −5.9 mA cm^{-2}, which is greater than those of NBSCF (−5.1 mA cm^{-2}) and BSCF (−4.8 mA cm^{-2}).

The long-term durability and stability of catalysts are critical factors for their practical applications in electrochemical devices. The durability of perovskite catalysts was investigated by cyclic voltammetry under accelerated degradation conditions in the potential range of 1.25 to 1.65 V for the OER and 0.6 to 1.2 V for the ORR at a scan rate of 200 mV s^{-1}. Figure 2 (A and B) shows the OER and ORR activities, respectively, of perovskite catalysts after durability tests as dashed lines. The OER durability of catalysts is presented as the increment of potential at 10 mA cm^{-2} after cycling 1500 times (Fig. 2C and Table 2). NBCFM exhibits the least potential increase of 17 mV, whereas BSCF shows a considerable decline of OER activity (26 mV). Similar to the OER durability results, NBCFM shows excellent long-term ORR durability, compared to NBSCF and BSCF, as revealed by the lowest potential differences at −3 mA cm^{-2} before and after the tests (Fig. 2, B and D, and Table 2). The potential of NBCFM at −3 mA cm^{-2} is decreased by 15 mV after cycling 10,000 times, whereas those of NBSCF and BSCF decrease considerably by 29 and 53 mV, respectively. Next, the long-term stability of the catalysts was investigated by the chronopotentiometric method, which

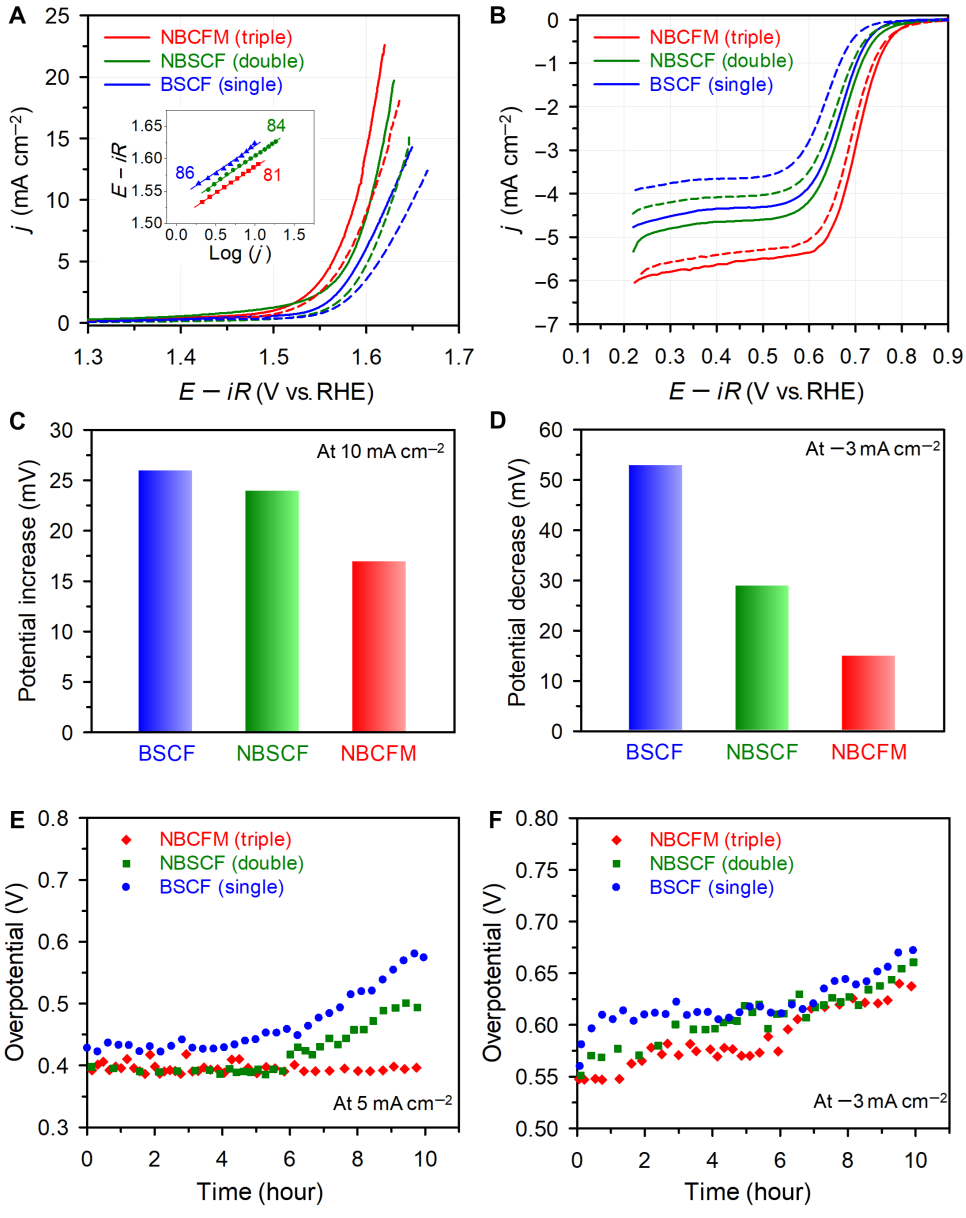

Fig. 2. Electrocatalytic activities and durabilities/stabilities of the perovskite catalysts. (**A**) OER polarization curves of BSCF, NBSCF, and NBCFM with corresponding Tafel plots (inset) before (solid line) and after (dashed line) the potential cycling. (**B**) ORR polarization curves of BSCF, NBSCF, and NBCFM before (solid line) and after (dashed line) potential cycling. (**C**) Potential increase of BSCF, NBSCF, and NBCFM at 10 mA cm^{-2} in OER after potential cycling. (**D**) Potential decreases of BSCF, NBSCF, and NBCFM at −3 mA cm^{-2} in ORR after potential cycling. (**E**) OER stabilities of BSCF, NBSCF, and NBCFM measured by chronopotentiometry at 5 mA cm^{-2} for 10 hours. (**F**) ORR stabilities of BSCF, NBSCF, and NBCFM measured by chronopotentiometry at −3 mA cm^{-2} for 10 hours.

was carried out at 5 mA cm^{-2} for the OER and −3 mA cm^{-2} for the ORR, at a rotation speed of 1600 rpm for 10 hours. As shown in Fig. 2E, the sudden potential increment is observed for BSCF and NBSCF after 4- and 6-hour testing, respectively, under the OER conditions, whereas NBCFM exhibits almost steady values of 0.395 V. However, in the ORR circumstances (Fig. 2F), NBCFM shows the steady increase of an overpotential of 9.0 mV $hour^{-1}$, which is similar to those of NBSCF (9.5 mV $hour^{-1}$) and BSCF (9.6 mV $hour^{-1}$).

The deterioration of perovskite-based catalysts during oxygen-involving reactions has seriously impeded their long-term use. In previous studies, thin amorphous layers were formed on the surfaces of perovskite-based catalysts during the OER cycles, resulting in suppression of the OER reaction with decreased current density (*22*, *23*). The declines of OER activities have been ascribed to surface amorphization phenomena with leaching of the A-site materials (for example, Ba or Sr). The structures of perovskite catalysts after the OER durability tests were observed with TEM imaging (fig. S4, A to C), which reveal formation of the thinnest amorphous layer on NBCFM among the three perovskite catalysts, suggesting the suppression of structural deterioration in the triple perovskite structure. The structural change of the perovskite catalysts under the OER conditions was further scrutinized with in situ x-ray absorption spectroscopy (XAS). Co K-edge x-ray absorption near-edge structure (XANES) spectra (fig. S4, D to F) show that all three perovskite catalysts undergo the shift of absorption edge

Table 2. Detailed data of electrocatalytic activities and durabilities for the perovskite-based catalysts with noble metal catalysts.

Catalyst	OER			ORR				$E_{OER} - E_{ORR}$ (V)
	E_{OER} at 10 mA cm^{-2} (V versus RHE)	Tafel slope (mV decade^{-1})	Potential increase at 10 mA cm^{-2} (mV)	E_{ORR} at −3 mA cm^{-2} (V versus RHE)	Tafel slope (mV decade^{-1})	j_d (mA cm^{-2})	Potential decrease at −3 mA cm^{-2} (mV)	
BSCF	1.625	86	26	0.641	64	−4.8	53	0.984
NBSCF	1.604	84	24	0.653	87	−5.1	29	0.951
NBCFM	1.589	81	17	0.698	63	−5.9	15	0.891
NBCFM/N-rGO	1.587	88	2	0.889	44	−6.2	14	0.698
Ir/C	1.561	70	92	0.792	–	–	–	0.769
Pt/C	1.695	–	–	0.894	40	−6.3	10	0.801

to higher energy under OER conditions (1.55 V versus RHE), with NBCFM exhibiting the smallest shift. The positive edge shift indicates the generation of Co species with a higher oxidation state, which could be associated with the formation of amorphous Co oxyhydroxide (*24*, *25*). The oxidation degree of the perovskite catalysts deduced from in situ XANES data is consistent with the generation of the surface amorphous layer observed with the TEM images after the OER durability tests. However, we note that the correlation of OER activity and amorphous layer formation shown by our perovskite catalysts is rather contradictory to a previous finding that the OER activity on BSCF increases with surface amorphization (*24*). In the context of the latter, Fabbri *et al.* (*25*) suggested that, by using time-resolved XAS measurements, changes in the electronic and local structures of catalysts under the OER conditions could be the origin of high OER activity. The OER activity trend of our perovskite catalysts appears more critically affected by the original crystal and electronic structures than the generation of the amorphous layer. Further work is necessary to clarify the degradation mechanism of perovskite-based catalysts in relation to the amorphization process under OER conditions. Overall, electrocatalytic performances of the perovskite catalysts demonstrate the promise of NBCFM triple perovskite as highly efficient and stable bifunctional catalysts for both ORR and OER.

High-performance NBCFM/N-rGO catalyst

Although the triple perovskite NBCFM demonstrated excellent oxygen electrode activity among the perovskite catalysts, its ORR activity is still relatively lower than the commercialized electrodes, primarily because of its low electrical conductivity. As a means of surmounting this limitation, we composited NBCFM with N-rGO, which can enhance the electrical conductivity, thereby boosting electrocatalytic activity. The hybridization was carried out by the hydrothermal reaction between GO and NBCFM at 180°C with urea (see Materials and Methods for details). During the reaction, the GO was transformed into N-rGO via urea-induced simultaneous reduction and nitrogen doping, thus affording an NBCFM/N-rGO hybrid. The characterization of the NBCFM/N-rGO composite catalyst is presented in fig. S5. In the NBCFM/N-rGO hybrid, NBCFM particles are uniformly distributed on the surfaces of N-rGO networks, as revealed by a TEM image (fig. S5A). The XRD peaks for NBCFM/N-rGO are well indexed as the triple perovskite phase without any extra peaks for other phases (fig. S5B), and the NBCFM/N-rGO shows a BET-specific surface area of 119.6 m^2 g^{-1} with a micropore volume of 0.345 cm^3 g^{-1} (fig. S5C). X-ray photoelectron spectroscopy (XPS) spectra for NBCFM/N-rGO (fig. S5, D and E) reveal the presence of all elements of the triple perovskite and the generation of nitrogen moieties, including pyridinic, pyrrolic, and graphitic nitrogen species. Raman spectra of GO and NBCFM/N-rGO (fig. S5G) suggest a relatively higher intensity of the D band in the NBCFM/N-rGO, indicating a partial loss of graphiticity during the hybridization and doping of nitrogen atoms (*26*).

We evaluated the bifunctional electrocatalytic activity of NBCFM/N-rGO for the OER and ORR (Fig. 3A and Table 2). For the OER, NBCFM/N-rGO reaches 10 mA cm^{-2} at an overpotential of 357 mV, similar to NBCFM. Notably, NBCFM/N-rGO exhibits a marked improvement in the ORR activity over NBCFM, with its potential at −3 mA cm^{-2} being 0.889 V. The ORR kinetics of NBCFM/N-rGO are also excellent, as its electron transfer number deduced from Koutecky-Levich analysis is 4.0 (fig. S5H). The bifunctional oxygen electrode activity of NBCFM/N-rGO was compared with those of the perovskite catalysts as well as benchmark catalysts, Ir/C for OER and Pt/C for ORR (Fig. 3, A and B, and Table 2). The oxygen electrode activity ($\Delta E = E_{OER} - E_{ORR}$) was calculated by subtracting the potential at −3 mA cm^{-2} for the ORR (E_{ORR}) from the potential at 10 mA cm^{-2} for the OER (E_{OER}). The ΔE values of the perovskite catalysts are 0.984, 0.951, and 0.891 V for BSCF, NBSCF, and NBCFM, respectively, indicating that NBCFM is the best-performing catalyst among the three perovskites. The ΔE is further reduced to 0.698 V with NBCFM/N-rGO, suggesting the promotion effects of both triple perovskite structure and hybridization with N-rGO. Notably, the oxygen electrode activity of NBCFM/N-rGO surpasses that of precious metal catalysts; ΔE values for Pt/C and Ir/C are 0.801 and 0.769 V, respectively. The extensive comparison of oxygen electrode activities of perovskite catalysts (*6*–*11*, *20*, *21*, *27*–*35*) reveals the NBCFM/N-rGO catalyst to be the best-performing perovskite-based, bifunctional oxygen electrocatalyst (Fig. 3C and table S2). Overall, the hybridization of NBCFM with N-rGO could exert a catalytic synergy, leading to highly efficient bifunctional electrocatalysis for the ORR and OER.

Next, the long-term durability and stability of the NBCFM/N-rGO catalyst were assessed (Fig. 3D and fig. S6). NBCFM/N-rGO exhibits only a slight increase in the potential of 2 mV at 10 mA cm^{-2} after cycling 1500 times in the range of 1.25 to 1.65 V (fig. S6A), which is

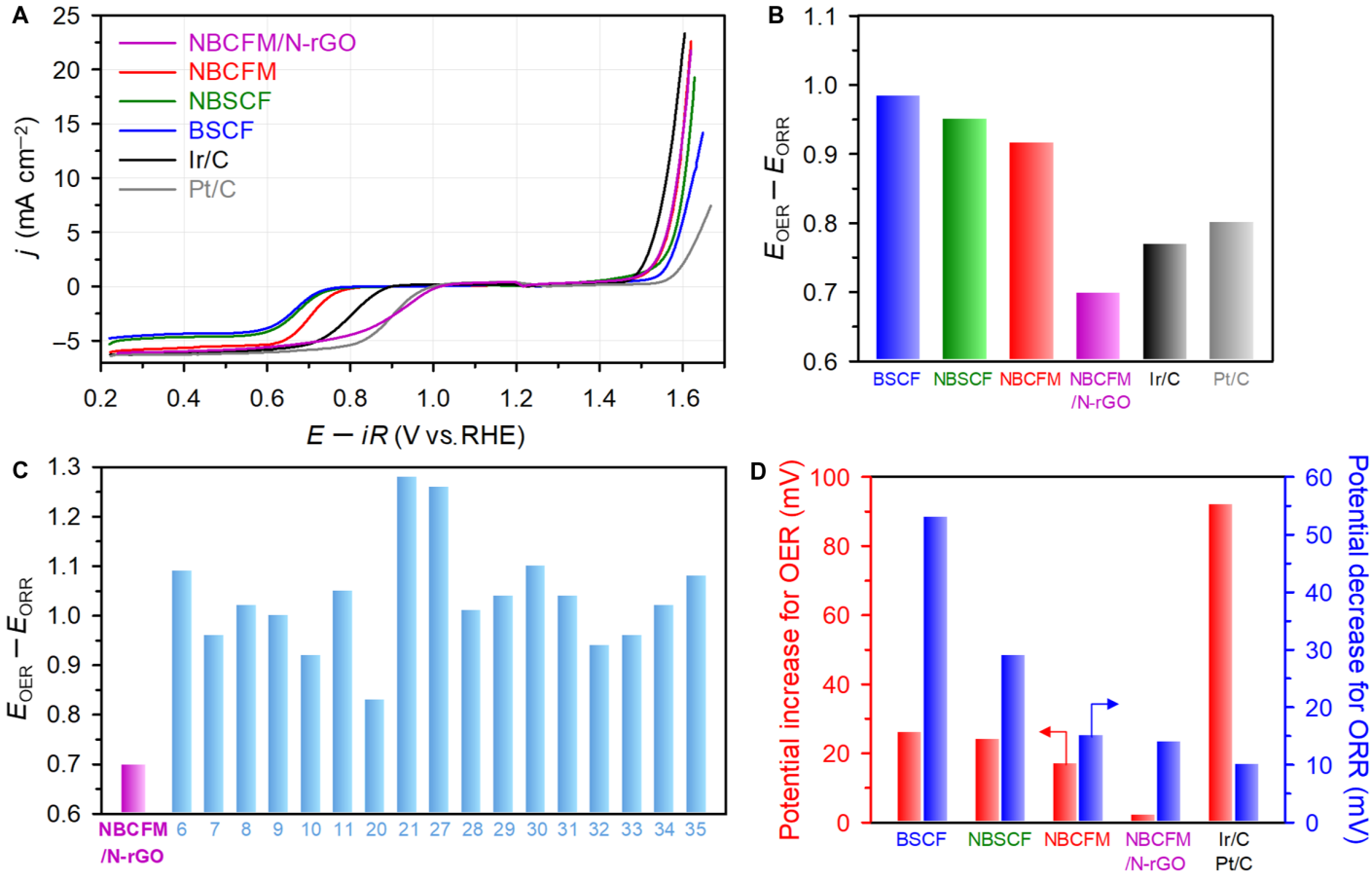

Fig. 3. Bifunctional oxygen electrode activities and durabilities of the perovskites, NBCFM/N-rGO, and precious metal catalysts. (**A**) OER/ORR polarization curves for perovskite-based catalysts and precious metal catalysts. (**B**) Oxygen electrode activities ($E_{OER} - E_{ORR}$) of perovskite-based catalysts and precious metal catalysts. (**C**) Comparisons of oxygen electrode activities of NBCFM/N-rGO with the previously reported bifunctional catalysts. The numbers on the *x* axis denote reference numbers. (**D**) OER potential increase and ORR potential decrease of perovskite-based catalysts and precious metal catalysts after durability tests.

significantly enhanced durability compared to NBCFM (17 mV). Moreover, after the 10-hour loading of 5 mA cm^{-2}, NBCFM/N-rGO exhibits a steady potential value of 0.405 V, which is much smaller than those for the BSCF, NBSCF, and Ir/C (fig. S6B). The durability of NBCFM/N-rGO is also pronounced for the ORR (Fig. 3D and fig. S6C); the potential of NBCFM/N-rGO at −3 mA cm^{-2} decreases by 14 mV after cycling 10,000 times in the range of 0.6 to 1.2 V. In addition, NBCFM/N-rGO shows a negligible change in the overpotential at −3 mA cm^{-2} for 10 hours, which is much lower than that of the three perovskite catalysts (fig. S6D). Notably, the TEM image of NBCFM/N-rGO after the OER durability test and in situ Co K-edge XANES spectrum of NBCFM/N-rGO at the OER potential reveal the formation of a thinner amorphous layer (fig. S6, E and F) on its surfaces than that generated on NBCFM (fig. S4, C and F), suggesting that the hybridization with N-rGO could suppress the amorphization-driven structural degradation. In the Co 2p XPS spectra (fig. S5F), the peaks (Co $2p_{3/2}$ and Co $2p_{1/2}$) of NBCFM/N-rGO are shifted by 0.8 eV to higher binding energies compared to peaks of NBCFM because of the mutual interaction between N-rGO and NBCFM, which evidences a strong hybridization of NBCFM particles with an N-rGO matrix (*36*). In addition, this electronic modification may stabilize the Co atoms, thereby inhibiting dissolution of NBCFM/N-rGO. The high surface area of N-rGO could provide better contact with the working electrode (glassy carbon), decreasing the probability of detachment (caused by evolved O_2) of the active particles during electrocatalysis.

Origin of the superior electrocatalytic performances of NBCFM

The superior electrocatalytic performances of NBCFM for oxygen electrode reactions may originate from two principal reasons: oxygen nonstoichiometry and electronic configuration. First, the unique triple perovskite structure produces ample oxygen vacancies, which play a deterministic role in their intrinsic OER/ORR activities because the type of lanthanide and oxidation state of B-site ions (Co, Fe, and Mn) affect the oxygen vacancy content (*24*). The oxygen vacancies can enhance the charge transfer reaction between adsorbate and adsorbent because they can behave as charged species. The nonstoichiometry δ values of BSCF, NBSCF, and NBCFM were determined to be 0.234, 0.379, and 0.495, respectively, as calculated from the cobalt oxidation state by using the iodometric titration method. The trend of δ values of the three perovskites is in agreement with the results of OER/ORR activity (Fig. 4A). The abundance of surface oxygen species of catalysts was further assessed by XPS (Fig. 4B and fig. S2, C to E). The observed O 1s XPS spectra are deconvoluted into two main components: the lower binding energy peak at approximately 529 eV is assigned to the lattice oxygen species (O^{2-}), while the higher peak at approximately 531 eV is

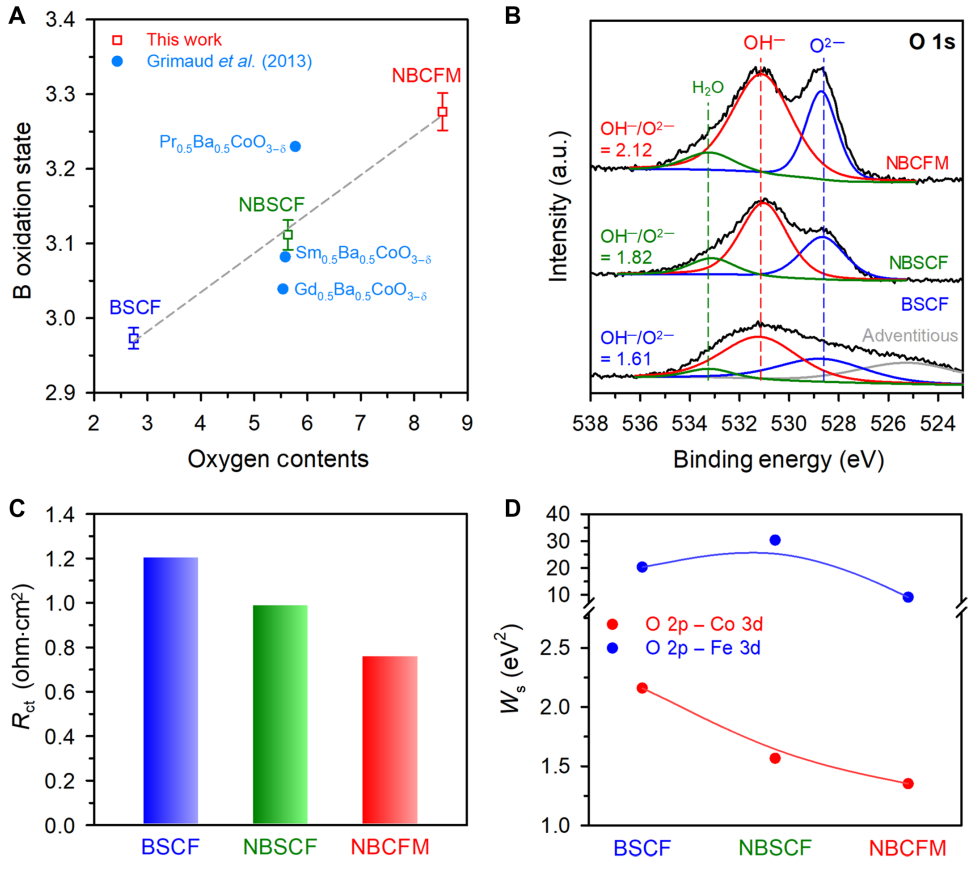

Fig. 4. Mechanistic insight into activity trends for oxygen electrode reactions. (**A**) Computed oxygen deficiency (δ) from the oxidation states of the B site in perovskite oxide materials using the iodometric titration method. (**B**) O 1s XPS spectra of BSCF, NBSCF, and NBCFM. (**C**) Charge-transport resistance values of the BSCF, NBSCF, and NBCFM. (**D**) Spectral weight (W_S) of charge transfer excitations from O 2p to Co 3d and Fe 3d electronic states for BSCF, NBSCF, and NBCFM. W_S is obtained from the optical conductivity spectra, as shown in fig. S8. A systematic and quantitative decrease of the hybridization between the Co and O states is observed from BSCF through NBSCF to NBCFM.

considered to be hydroxyl groups (OH^-). NBCFM exhibits the highest value of 2.12 for the ratio of OH^-/O^{2-} among the perovskite-based catalysts (NBSCF, 1.82; BSCF, 1.61). The higher concentration of surface OH^- species in NBCFM implies the generation of a high density of extra oxygen vacancies by lanthanide ions, which may be responsible for the faster reaction rate of NBCFM for oxygen electrode reactions (*15*, *27*).

The OER mechanism comprises multiple steps according to the theory of Krasil'shchikov (*37*), and the detailed equations can be written as

$$S + OH^- \rightarrow S - OH + e^- \quad (1)$$

$$S - OH + OH^- \rightarrow S - O^- + H_2O(l) \quad (2)$$

$$S - O^- \rightarrow S - O + e^- \quad (3)$$

$$2S - O \rightarrow 2S + O_2(g) \quad (4)$$

where *S* represents an electrochemical active site for the OER. The above equations imply that many different types of active sites can promote the overall electrochemical reaction kinetics. Along with the generation of oxygen deficiency in the perovskite structure, the substitution of the A- and B-site metal cations can also significantly affect their electronic structures and coordination chemistry (*28*). The large difference in the ionic radius between Nd^{3+} and Ba^{2+} results in the oxygen deficiency in the triple perovskite being localized in the lanthanide planes. In addition, the interactions between B-site multivalent ions (Co^{3+}/Co^{4+}, Fe^{3+}/Fe^{4+}, and Mn^{3+}/Mn^{4+}), with different electronic structures in the crystal lattice, provide plenty of active sites favorable for the OER/ORR (fig. S2, C to E).

To confirm our explanation that the greater covalency of transition metal cation–oxygen bonds in NBCFM expedites the charge transfer between redox-active centers and reactants for OER/ORR, we exploited the electrochemical impedance spectroscopy (EIS) technique to analyze the resistance components. Figure S7A shows the complex-plane Nyquist plots of BSCF, NBSCF, NBCFM, and NBCFM/N-rGO in 0.1 M KOH solution at a current density of 10 mA cm^{-2}. The resistance components of catalysts are separated as the ohmic (R_{ohmic}), charge-transport (R_{ct}), and mass-transport (R_{mt}) resistances from the fitted equivalent circuit using EC-Lab software (*8*). The values of R_{ct} are obtained from the Nyquist plots in the high-frequency region. NBCFM shows the lowest R_{ct} value among the three perovskites, and NBCFM/N-rGO exhibits an even lower R_{ct} value compared to NBCFM (Fig. 4C and fig. S7, B to D). The R_{ct} values are 1.20, 0.99, 0.76, and 0.08 ohm·cm^2 for BSCF, NBSCF, NBCFM, and NBCFM/N-rGO, respectively. Furthermore, the steeper line of NBCFM/N-rGO at low frequency demonstrates a faster kinetics of the diffusion process (fig. S7C) (*38*), indicating that the unit cell structure, as well as the hybridization with N-rGO

support, greatly affects the charge transfer kinetics of the perovskite-based catalysts. In contrast, the R_{ohmic} values of the catalysts are almost invariant among the perovskite catalysts.

We next assessed the impact of the electronic configurations of the perovskite catalysts on the oxygen electrode activities. As descriptors for the OER/ORR activity, the electronic structures of catalysts, such as the electron occupancy of the transition metal e_g orbitals, the proximity of the O p band to the Fermi energy (E_F), and the surface binding strength of oxygen-related intermediates, have been considered for the efficient design of oxide electrocatalysts, as reported earlier (*12*, *13*). In particular, elemental defects in perovskite oxides can significantly affect the electronic structure through modifications in chemical bonding and hybridization between the transition metal 3d and O 2p orbitals. Figure S8 shows optical spectra, that is, real [$\varepsilon_1(\omega)$] and imaginary [$\varepsilon_2(\omega)$] parts of the dielectric functions and optical conductivity [$\sigma_1(\omega)$] obtained by spectroscopic ellipsometry, which reveals the electronic structure near the E_F. The systematic changes of the electronic structure can be understood by considering how the crystalline symmetry changes with the elemental vacancy concentration. We can quantitatively estimate the hybridization strength between the transition metal 3d and O 2p states by analyzing $\sigma_1(\omega)$. On the basis of the energy consideration and previous first-principles calculation results on perovskite materials (*16*, *39*), the lowest lying absorption of around ~1 eV, which is common for all the samples, corresponds to the charge transfer excitation between the Co 3d and O 2p states. The second, larger absorption near ~2.5 eV can be attributed to the charge transfer excitation between Fe 3d and O 2p states. The optical measurement shown here provides quantitative information on the charge transfer excitation, which other spectroscopic techniques, such as x-ray absorption and photoemission spectroscopy, cannot deliver. The charge transfer excitations can be considered as a direct and quantitative measure for the hybridization between the transition metal and oxygen. As shown in Fig. 4D, the hybridization strength obtained from the spectral weight of the lowest lying absorption peaks (O 2p–Co 3d) is systematically smaller for NBCFM, indicating smaller covalency. This is consistent with the abundant oxygen vacancy concentration, as well as the low R_{ct} values observed for the NBCFM catalyst. In addition, the overall hybridization strength for Fe/O is much larger than that for Co/O, suggesting that Co states are more relevant in influencing the electrochemical activities, as previously discussed (*12*, *13*, *15*, *38*).

DISCUSSION

We have demonstrated that the triple perovskite NBCFM exhibits an excellent electrocatalytic activity and durability/stability for oxygen electrode reactions. The repeated stacking of lanthanide causes structural distortion of the lattice in the NBCFM triple perovskite, generating extra oxygen vacancies, compared to BSCF and NBSCF. The extra oxygen vacancies in NBCFM play an important role in boosting the catalytic activity and durability/stability of NBCFM for the OER and ORR, which are superior to those of BSCF and NBSCF. Significantly, when NBCFM was hybridized with N-rGO, the resulting NBCFM/N-rGO exhibits the best oxygen electrode activity ever reported among perovskite-based catalysts. The enhancement of oxygen electrode activity by NBCFM could be attributed to its oxygen defect–rich structure, the low charge resistance, and the small covalency between O 2p and Co 3d orbitals. Overall, we believe that the structural engineering of perovskites is an effective means of boosting the performances of perovskite-based catalysts. The newly developed triple perovskite NBCFM catalyst can find widespread utility in a range of energy devices, such as unitized regenerative fuel cells and intermediate temperature–reversible solid oxide fuel cells.

MATERIALS AND METHODS

Synthesis and characterization of perovskite catalysts

The perovskite-based BSCF (single), NBSCF (double), and NBCFM (triple) catalysts were synthesized by the glycine-nitrate combustion method. Stoichiometric amounts of metal nitrate precursors, such as $Nd(NO_3)_3{\cdot}6H_2O$ (Alfa Aesar), $Ba(NO_3)_2$ (Alfa Aesar), $Sr(NO_3)_2$ (Alfa Aesar), $Mn(NO_3)_2{\cdot}xH_2O$ (Alfa Aesar), $Co(NO_3)_3{\cdot}6H_2O$ (Sigma-Aldrich), and $Fe(NO_3)_3{\cdot}9H_2O$ (Duksan), were dissolved in distilled water (>18 megohms·cm). Then, an appropriate amount of glycine (Alfa Aesar) was added into the solution with heating and vigorous stirring on a hot plate, until black ash was formed. Each prepared ash was ground by using a mortar and pestle, precalcined at 600°C for 4 hours, and then ball-milled in ethanol for 24 hours using a zirconia ball. The ball-milled catalysts were dried in an electric oven at 60°C for 10 hours and then calcined at 900° to 1200°C for 4 hours to obtain a pure phase of perovskite.

NBCFM/N-rGO materials were synthesized by the hydrothermal reaction. GO was prepared from graphite powder (Sigma-Aldrich) by the modified Hummers method. The as-prepared GO was mixed with deionized (DI) water, urea (Samchun Chemicals), and NBCFM in a Teflon beaker and then heated at 180°C for 12 hours in a stainless steel autoclave. The products were washed using DI water, filtrated to remove any residual materials several times, and then dried on a hot plate.

The phase constitution and crystal structure were analyzed by powder XRD (Cu-Kα radiation, D/MAX 2500, Rigaku) and high-resolution synchrotron XRD at the 9B beamline of the Pohang Light Source (PLS-II). XRD Rietveld structural refinement was conducted via FullProf software. The microstructures were investigated by FESEM (JEOL JSM-6500F, 10 kV) and HRTEM (FEI Titan Cubed G2 60-300, 300 kV). The chemical compositions of component phases were analyzed using an EDX system equipped to the HRTEM. The porous structure of catalysts was analyzed by equation using a 3Flex surface characterization analyzer (Micromeritics). The specific surface area of catalysts was calculated by the BET equation, and their pore size distribution was calculated by the Barrett-Joyner-Halenda method from the adsorption branch of the isotherm.

Electrochemical measurements of oxygen electrode reactions

The electrochemical analysis of perovskite-based catalysts was performed using a potentiostat/galvanostat electrochemical analyzer (SP-150, Bio-Logic) equipped with an RDE system (RRDE-3A, ALS). The three-electrode electrochemical cell was composed of an Hg/HgO (1 M NaOH) reference electrode, a graphite rod counter electrode, and the perovskite-based catalyst-coated glassy carbon working electrode. To prepare a catalyst ink, 10.0 mg of catalyst powder and 5.0 mg of Vulcan XC-72 (Cabot) were dispersed in a mixture of 750 μl of DI water, 250 μl of isopropanol, and 16 μl of aqueous Nafion solution (Sigma-Aldrich) in a glass vial (DAIHAN Scientific); the mixed suspension was then sonicated for 30 min to form a homogeneous ink. The electrolyte (0.1 M KOH solution) was prepared using a potassium hydroxide pellet (Daejung). All the potentials measured were converted to the RHE scale.

Before measuring the activity of oxygen electrode reactions, cyclic voltammetry was performed between 0.05 and 1.2 V for 50 cycles at

a scan rate of 100 mV s^{-1} to clean the surface of the catalyst. For the OER and ORR activity measurements, linear sweep voltammetry (LSV) was conducted using the RDE in N_2-saturated 0.1 M KOH solution from 1.2 to 1.7 V (scan rate of 5 mV s^{-1} with 1600 rpm) for OER and in an O_2-saturated electrolyte from 1.2 to 0.2 V (scan rate of 5 mV s^{-1} with 400, 900, 1600, and 2500 rpm) versus RHE for ORR. The long-term durability of the catalysts was investigated by obtaining LSV curves before and after the potential sweep between 1.25 and 1.65 V for 1500 cycles (scan rate of 200 mV s^{-1}) for OER and between 0.6 and 1.2 V for 10,000 cycles (scan rate of 200 mV s^{-1}) for ORR. The steady-state polarization stability was tested by the chronopotentiometric method for 10 hours at 5 mA cm^{-2} (OER) and −3 mA cm^{-2} (ORR). Ohmic losses were corrected by the *iR*-interruption method by SP-150 EIS. The EIS was performed in the frequency range (100 kHz to 100 mHz) at the fixed amplitude of 10 mV. An appropriate equivalent circuit model was fitted using EC-Lab software to calculate the resistance components of materials.

XAS experiments

XAS experiments were performed on the Beamline 8C of the Pohang Accelerator Laboratory in the Republic of Korea with a beam energy and current of 3 GeV and 360 mA, respectively. Catalyst ink composed of the catalyst powder, Vulcan XC-72, DI water, Nafion, and isopropanol was deposited onto a piece of carbon paper (0.8 cm × 1.0 cm), resulting in the catalyst loading of 0.1 to 0.2 mg cm^{-2}. The as-deposited catalyst film was attached onto the window of a homemade polytetrafluoroethylene-based spectroelectrochemical cell and subjected to an XAS measurement with a fluorescent detection mode. After the first measurement, 0.1 M KOH was poured into the cell, and a graphite rod counter electrode and Hg/HgO reference electrode were equipped. EIS was performed at around open circuit potential to obtain series resistance. Finally, a constant potential of 1.55 V (versus RHE, 90% *iR*-compensated) was applied, and a single XAS measurement was carried out after 10 min. The background correction and normalization of raw XAS data were performed using IFEFFIT (Athena) software (*40*).

Determination of oxygen nonstoichiometry

The oxygen nonstoichiometry (δ) of catalysts at room temperature was determined by the iodometric titration method. Twenty milligrams of powder was dissolved in 10 ml of 3.5 N HCl. To this solution, 20 ml of potassium iodide (KI; Daejung) was added with a tiny amount of starch as an indicator using a small magnetic bar. Then, the solution was titrated with 0.025 N sodium thiosulfate ($Na_2S_2O_3$; Daejung), until the solution color began to transform.

The chemical identification and electronic structure of all the elements in the catalysts were determined by XPS (VG ESCALAB 220i) analysis using an Al Kα x-ray source ($h\nu$ = 1486.6 eV). The oxygen species on the catalyst surface were also analyzed, and the atomic ratio of hydroxyl groups (OH^-) and lattice oxygen (O^{2-}) was calculated to obtain the relative amount of oxygen vacancies in the oxygen lattice.

Spectroscopic ellipsometry

For the optical measurements, the perovskite-based catalysts were polished to optical grade. A spectroscopic ellipsometer (VASE, J. A. Woollam Co.) was used to collect optical spectra at room temperature between photon energies of 0.74 and 5.50 eV. Incident angles of 65°, 70°, and 75° were used. A single-layer model was sufficient to obtain physically reasonable optical spectra, and the surface roughness layer did not influence the result significantly.

SUPPLEMENTARY MATERIALS

Supplementary material for this article is available at http://advances.sciencemag.org/cgi/content/full/4/6/eaap9360/DC1

fig. S1. Structural and elemental analyses of the perovskite catalysts.
fig. S2. Nitrogen adsorption-desorption and XPS analysis of the perovskite catalysts.
fig. S3. ORR activity of the perovskite catalysts.
fig. S4. Structural changes of the perovskite catalysts after or during the OER.
fig. S5. Physicochemical and electrochemical characterizations of the NBCFM/N-rGO catalyst.
fig. S6. Long-term durability and stability of catalysts for OER and ORR.
fig. S7. EIS analysis of the perovskite-based catalysts.
fig. S8. Optical properties and electronic structures of the perovskite-based catalysts.
table S1. Textural properties of the perovskite-based catalysts.
table S2. Comparison of the OER/ORR bifunctional activity of NBCFM/N-rGO with the reported bifunctional perovskite catalysts.

REFERENCES AND NOTES

1. V. R. Stamenkovic, D. Strmcnik, P. P. Lopes, N. M. Markovic, Energy and fuels from electrochemical interfaces. *Nat. Mater.* **16**, 57–69 (2016).
2. S. Park, Y. Shao, J. Liu, Y. Wang, Oxygen electrocatalysts for water electrolyzers and reversible fuel cells: Status and perspective. *Energy Environ. Sci.* **5**, 9331–9344 (2012).
3. I. Katsounaros, S. Cherevko, A. R. Zeradjanin, K. J. J. Mayrhofer, Oxygen electrochemistry as a cornerstone for sustainable energy conversion. *Angew. Chem. Int. Ed.* **53**, 102–121 (2014).
4. D. Chen, C. Chen, Z. M. Baiyee, Z. Shao, F. Ciucci, Nonstoichiometric oxides as low-cost and highly-efficient oxygen reduction/evolution catalysts for low-temperature electrochemical devices. *Chem. Rev.* **115**, 9869–9921 (2015).
5. M. Kuang, G. Zheng, Nanostructured bifunctional redox electrocatalysts. *Small* **12**, 5656–5675 (2016).
6. Y. Zhao, L. Xu, L. Mai, C. Han, Q. An, X. Xu, X. Liu, Q. Zhang, Hierarchical mesoporous perovskite $La_{0.5}Sr_{0.5}CoO_{2.91}$ nanowires with ultrahigh capacity for Li-air batteries. *Proc. Natl. Acad. Sci. U.S.A.* **109**, 19569–19574 (2012).
7. Z. Chen, A. Yu, D. Higgins, H. Li, H. Wang, Z. Chen, Highly active and durable core–corona structured bifunctional catalyst for rechargeable metal–air battery application. *Nano Lett.* **12**, 1946–1952 (2012).
8. W. G. Hardin, D. A. Slanac, X. Wang, S. Dai, K. P. Johnston, K. J. Stevenson, Highly active, nonprecious metal perovskite electrocatalysts for bifunctional metal–air battery electrodes. *J. Phys. Chem. Lett.* **4**, 1254–1259 (2013).
9. J.-I. Jung, H. Y. Jeong, J.-S. Lee, M. G. Kim, J. Cho, A bifunctional perovskite catalyst for oxygen reduction and evolution. *Angew. Chem. Int. Ed.* **53**, 4582–4586 (2014).
10. H. W. Park, D. U. Lee, P. Zamani, M. H. Seo, L. F. Nazar, Z. Chen, Electrospun porous nanorod perovskite oxide/nitrogen-doped graphene composite as a bi-functional catalyst for metal air batteries. *Nano Energy* **10**, 192–200 (2014).
11. M. Prabu, P. Ramakrishnan, P. Ganesan, A. Manthiram, S. Shanmugam, $LaTi_{0.65}Fe_{0.35}O_{3-\delta}$ nanoparticle-decorated nitrogen-doped carbon nanorods as an advanced hierarchical air electrode for rechargeable metal-air batteries. *Nano Energy* **15**, 92–103 (2015).
12. J. Suntivich, K. J. May, H. A. Gasteiger, J. B. Goodenough, Y. Shao-Horn, A perovskite oxide optimized for oxygen evolution catalysis from molecular orbital principles. *Science* **334**, 1383–1385 (2011).
13. J. Suntivich, H. A. Gasteiger, N. Yabuuchi, H. Nakanishi, J. B. Goodenough, Y. Shao-Horn, Design principles for oxygen-reduction activity on perovskite oxide catalysts for fuel cells and metal–air batteries. *Nat. Chem.* **3**, 546–550 (2011).
14. A. Grimaud, K. J. May, C. E. Carlton, Y.-L. Lee, M. Risch, W. T. Hong, J. Zhou, Y. Shao-Horn, Double perovskites as a family of highly active catalysts for oxygen evolution in alkaline solution. *Nat. Commun.* **4**, 2439 (2013).
15. N.-I. Kim, R. A. Afzal, S. R. Choi, S. W. Lee, D. Ahn, S. Bhattacharjee, S.-C. Lee, J. H. Kim, J.-Y. Park, Highly active and durable nitrogen doped-reduced graphene oxide/double perovskite bifunctional hybrid catalysts. *J. Mater. Chem. A* **5**, 13019–13031 (2017).
16. S. A. Lee, S. Oh, J.-Y. Hwang, M. Choi, C. Youn, J. W. Kim, S. H. Chang, S. Woo, J.-S. Bae, S. Park, Y.-M. Kim, S. Lee, T. Choi, S. W. Kim, W. S. Choi, Enhanced electrocatalytic activity *via* phase transitions in strongly correlated $SrRuO_3$ thin films. *Energy Environ. Sci.* **10**, 924–930 (2017).
17. X. Cheng, E. Fabbri, M. Nachtegaal, I. E. Castelli, M. E. Kazzi, R. Haumont, N. Marzari, T. J. Schmidt, Oxygen evolution reaction on $La_{1-x}Sr_xCoO_3$ perovskites: A combined experimental and theoretical study of their structural, electronic, and electrochemical properties. *Chem. Mater.* **27**, 7662–7672 (2015).
18. R. Beyers, T. M. Shaw, The structure of $Y_1Ba_2Cu_3O_{7-\delta}$ and its derivatives. *Solid State Phys.* **42**, 135–212 (1989).
19. F. Dong, M. Ni, Y. Chen, D. Chen, M. O. Tadé, Z. Shao, Structural and oxygen-transport studies of double perovskites $PrBa_{1-x}Co_2O_{5+\delta}$ (x = 0.00, 0.05, and 0.10) toward their application as superior oxygen reduction electrodes. *J. Mater. Chem. A* **2**, 20520–20529 (2014).

20. K. Elumeena, J. Masa, F. Tietz, F. Yang, W. Xia, M. Muhler, W. Schuhmann, A simple approach towards high-performance perovskite-based bifunctional oxygen electrocatalysts. *ChemElectroChem* **3**, 138–143 (2016).
21. Z. Wang, Y. You, J. Yuan, Y.-X. Yin, Y.-T. Li, S. Xin, D. Zhang, Nickel-doped $La_{0.8}Sr_{0.2}Mn_{1-x}Ni_xO_3$ nanoparticles containing abundant oxygen vacancies as an optimized bifunctional catalyst for oxygen cathode in rechargeable lithium–air batteries. *ACS Appl. Mater. Interfaces* **8**, 6520–6528 (2016).
22. D. He, G. He, H. Jiang, Z. Chen, M. Huang, Enhanced durability and activity of the perovskite electrocatalyst $Pr_{0.5}Ba_{0.5}CoO_{3-\delta}$ by Ca doping for the oxygen evolution reaction at room temperature. *Chem. Commun.* **53**, 5132–5135 (2017).
23. S. Yagi, I. Yamada, H. Tsukasaki, A. Seno, M. Murakami, H. Fujii, H. Chen, N. Umezawa, H. Abe, N. Nishiyama, S. Mori, Covalency-reinforced oxygen evolution reaction catalyst. *Nat. Commun.* **6**, 8249 (2015).
24. K. J. May, C. E. Carlton, K. A. Stoerzinger, M. Risch, J. Suntivich, Y.-L. Lee, A. Grimaud, Y. Shao-Horn, Influence of oxygen evolution during water oxidation on the surface of perovskite oxide catalysts. *J. Phys. Chem. Lett.* **3**, 3264–3270 (2012).
25. E. Fabbri, M. Nachtegaal, T. Binninger, X. Cheng, B.-J. Kim, J. Durst, F. Bozza, T. Graule, R. Schäublin, L. Wiles, M. Pertoso, N. Danilovic, K. E. Ayers, T. J. Schmidt, Dynamic surface self-reconstruction is the key of highly active perovskite nano-electrocatalysts for water splitting. *Nat. Mater.* **16**, 925–931 (2017).
26. S. Bag, K. Roy, C. S. Gopinath, C. R. Raj, Facile single-step synthesis of nitrogen-doped reduced graphene oxide-Mn_3O_4 hybrid functional material for the electrocatalytic reduction of oxygen. *ACS Appl. Mater. Interfaces* **6**, 2692–2699 (2014).
27. Y. Zhu, W. Zhou, J. Yu, Y. Chen, M. Liu, Z. Shao, Enhancing electrocatalytic activity of perovskite oxides by tuning cation deficiency for oxygen reduction and evolution reactions. *Chem. Mater.* **28**, 1691–1697 (2016).
28. J.-I. Jung, M. Risch, S. Park, M. G. Kim, G. Nam, H.-Y. Jeong, Y. Shao-Horn, J. Cho, Optimizing nanoparticle perovskite for bifunctional oxygen electrocatalysis. *Energy Environ. Sci.* **9**, 176–183 (2016).
29. W. Zhou, J. Sunarso, Enhancing bi-functional electrocatalytic activity of perovskite by temperature shock: A case study of $LaNiO_{3-\delta}$. *J. Phys. Chem. Lett.* **4**, 2982–2988 (2013).
30. D. Zhang, Y. Song, Z. Du, L. Wang, Y. Li, J. B. Goodenough, Active $LaNi_{1-x}Fe_xO_3$ bifunctional catalysts for air cathodes in alkaline media. *J. Mater. Chem. A* **3**, 9421–9426 (2015).
31. G. Liu, H. Chen, L. Xia, S. Wang, L.-X. Ding, D. Li, K. Xiao, S. Dai, H. Wang, Hierarchical mesoporous/macroporous perovskite $La_{0.5}Sr_{0.5}CoO_{3-x}$ nanotubes: A bifunctional catalyst with enhanced activity and cycle stability for rechargeable lithium oxygen batteries. *ACS Appl. Mater. Interfaces* **7**, 22478–22486 (2015).
32. D. U. Lee, H. W. Park, M. G. Park, V. Ismayilov, Z. Chen, Synergistic bifunctional catalyst design based on perovskite oxide nanoparticle and intertwined carbon nanotubes for rechargeable zinc–air battery applications. *ACS Appl. Mater. Interfaces* **7**, 902–910 (2015).
33. X. Ge, F. W. T. Goh, B. Li, T. S. A. Hor, J. Zhang, P. Xiao, X. Wang, Y. Zong, Z. Liu, Efficient and durable oxygen reduction and evolution of a hydrothermally synthesized $La(Co_{0.55}Mn_{0.45})_{0.99}O_{3-\delta}$ nanorod/graphene hybrid in alkaline media. *Nanoscale* **7**, 9046–9054 (2015).
34. C. Kim, O. Gwon, I.-Y. Jeon, Y. Kim, J. Shin, Y.-W. Ju, J.-B. Baek, G. Kim, Cloud-like graphene nanoplatelets on $Nd_{0.5}Sr_{0.5}CoO_{3-\delta}$ nanorods as an efficient bifunctional electrocatalyst for hybrid Li–air batteries. *J. Mater. Chem. A* **4**, 2122–2127 (2016).
35. X. Han, F. Cheng, T. Zhang, J. Yang, Y. Hu, J. Chen, Hydrogenated uniform Pt clusters supported on porous $CaMnO_3$ as a bifunctional electrocatalyst for enhanced oxygen reduction and evolution. *Adv. Mater.* **26**, 2047–2051 (2014).
36. Y. Liang, Y. Li, H. Wang, J. Zhou, J. Wang, T. Regier, H. Dai, Co_3O_4 nanocrystals on graphene as a synergistic catalyst for oxygen reduction reaction. *Nat. Mater.* **10**, 780–786 (2011).
37. A. I. Krasil'shchikov, On the intermediate stages of anodic oxygen evolution. *Zh. Fiz. Khim.* **37**, 531–537 (1963).
38. D. He, Y. Jiang, H. Lv, M. Pan, S. Mu, Nitrogen-doped reduced graphene oxide supports for noble metal catalysts with greatly enhanced activity and stability. *Appl. Catal. B* **132–133**, 379–388 (2013).
39. E. A. Kotomin, Yu. A. Mastrikov, M. M. Kuklja, R. Merkle, A. Roytburd, J. Maier, First principles calculations of oxygen vacancy formation and migration in mixed conducting $Ba_{0.5}Sr_{0.5}Co_{1-y}Fe_yO_{3-\delta}$ perovskites. *Solid State Ionics* **188**, 1–5 (2011).
40. B. Ravel, M. Newville, *ATHENA, ARTEMIS, HEPAESTUS*: Data analysis for X-ray absorption spectroscopy using *IFEFFIT*. *J. Synchrotron Radiat.* **12**, 537–541 (2005).

Acknowledgments

Funding: This research was supported by the Mid-Career Researcher Program (NRF-2017R1A2A2A05069812, NRF-2017R1A2B4011083, NRF-2017R1A2B2008464, and 2016K1A3A1A21004685), Climate Change Technology Research Program (NRF-2015M1A2A2057042), and Basic Research Laboratory Program (NRF-2017R1A4A1015564) through the National Research Foundation of Korea and by the International Collaborative Energy Technology R&D Program of the Korea Institute of Energy Technology Evaluation and Planning granted financial resource from the Ministry of Trade, Industry and Energy, Korea (no. 20158520030830). **Author contributions:** N.-I.K., S.H.J., and J.-Y.P. designed the experiments. N.-I.K., Y.J.S., S.R.C., and R.A.A. performed the synthesis of catalysts and physicochemical and electrochemical analyses. Y.-S.S. synthesized the GO solution for NBCFM/N-rGO. T.S.Y., T.C., and W.S.C. measured the optical conductivities and calculated the bandgap energies of the samples. Y.J.S. and K.-S.L. carried out the in situ XAS analyses. J.Y.H. analyzed the crystalline structures of the catalysts via TEM investigation. N.-I.K., Y.J.S., W.S.C., S.H.J., and J.-Y.P. wrote the paper. All authors contributed to writing and editing the document. **Competing interests:** The authors declare that they have no competing interests. **Data and materials availability:** All data needed to evaluate the conclusions in the paper are present in the paper and/or the Supplementary Materials. Additional data related to this paper may be requested from the corresponding authors.

Submitted 12 September 2017
Accepted 27 April 2018
Published 15 June 2018
10.1126/sciadv.aap9360

Citation: N.-I. Kim, Y. J. Sa, T. S. Yoo, S. R. Choi, R. A. Afzal, T. Choi, Y.-S. Seo, K.-S. Lee, J. Y. Hwang, W. S. Choi, S. H. Joo, J.-Y. Park, Oxygen-deficient triple perovskites as highly active and durable bifunctional electrocatalysts for oxygen electrode reactions. *Sci. Adv.* **4**, eaap9360 (2018).

ScienceAdvances

Oxygen-deficient triple perovskites as highly active and durable bifunctional electrocatalysts for oxygen electrode reactions

Nam-In Kim, Young Jin Sa, Tae Sup Yoo, Sung Ryul Choi, Rana Arslan Afzal, Taekjib Choi, Young-Soo Seo, Kug-Seung Lee, Jun Yeon Hwang, Woo Seok Choi, Sang Hoon Joo and Jun-Young Park

Sci Adv **4** (6), eaap9360.
DOI: 10.1126/sciadv.aap9360